ACS APPLIED MATERIALS & INTERFACES

Research Article

Cite This: ACS Appl. Mater. Interfaces 2017, 9, 39425-39431

www.acsami.org

Facet-Selective Deposition of FeO_x on α-MoO_3 Nanobelts for Lithium Storage

Yao Yao,[†,§] Nuo Xu,[‡,§] Doudou Guan,[†] Jiantao Li,[†] Zechao Zhuang,[†] Liang Zhou,*[,†] Changwei Shi,[†] Xue Liu,[†] and Liqiang Mai*[,†]

[†]State Key Laboratory of Advanced Technology for Materials Synthesis and Processing, Wuhan University of Technology, Hubei, Wuhan 430070, China

[‡]School of Chemistry, Chemical Engineering and Life Sciences, Wuhan University of Technology, Hubei, Wuhan 430070, China

Supporting Information

ABSTRACT: One-dimensional heterostructures have attracted significant interests in various applications. However, the selective deposition of shell material on specific sites of the backbone material remains a challenge. Herein, a facile facet-selective deposition strategy has been developed for the construction of heterostructured α-MoO_3@FeO_x nanobelts. Because of the anisotropic feature of α-MoO_3 nanobelts, the FeO_x nanoparticles selectively deposit on the edges of α-MoO_3 nanobelts, that is, the {100} and {001} facets. Such a heterostructure facilitates the electron transfer in lithium storage. As a result, the α-MoO_3@FeO_x nanobelts exhibit high capacities of 913 mA h g^{-1} after 100 cycles at 200 mA g^{-1} and 540 mA h g^{-1} after 100 cycles at 1000 mA g^{-1}. The facet-selective deposition strategy developed here would be extended to the construction of other novel heterostructures with fascinating physical/chemical properties and wide potential applications.

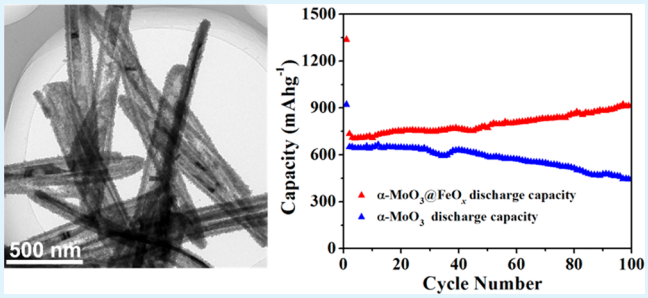

KEYWORDS: *α-MoO_3 nanobelts, FeO_x, facet-selective deposition, anode materials, lithium storage*

INTRODUCTION

One-dimensional (1D) heterostructures have the potential to integrate the merits of different components and 1D structures into one entity, endowing the material with multifunctionalities. In addition, the composite structure may lead to a synergistic effect on the physical/chemical properties. Therefore, the 1D heterostructures attract significant scientific and technological interests in electronics, photovoltaics, gas sensors, as well as energy storage and conversion.[1−7]

Various 1D heterostructures have been designed and constructed for energy storage. For example, Mai et al. synthesized $MnMoO_4$/$CoMoO_4$ hierarchical nanowires with improved supercapacitor performance.[8] Lou and co-workers prepared CNT@TiO_2 and CNT@SnO_2 1D hierarchical structures, and the heterostructures show enhanced lithium storage performances.[9] Fan et al. grew Co_3O_4@NiO, and ZnO@NiO core@shell nanowire arrays on a variety of conductive substrates; the Co_3O_4@NiO nanowire arrays on Ni foam display excellent supercapacitor performance.[10] The same group also reported the synthesis of Co_3O_4@$Co(OH)_2$ and Co_3O_4@$Mn(OH)_2$ core@shell nanowire arrays.[11] Liu et al. constructed CoO@polypyrrole nanowire arrays on Ni foam with boosted pseudocapacitive performance.[12] In all of these cases, the shell material coats on the backbone material uniformly. However, the preferential growth of the shell material on specific sites of the backbone material remains a challenge.

In our work, we develop a facet-selective deposition strategy to construct novel heterostructured α-MoO_3@FeO_x nanobelts. The growth of amorphous FeO_x nanoparticles on α-MoO_3 nanobelts is achieved by the hydrolysis and oxidation of ferrous ions under mild conditions. Because of the anisotropic feature of α-MoO_3 nanobelts, the amorphous FeO_x nanoparticles selectively deposit on the high-energy {001} and {100} facets of α-MoO_3. The resultant α-MoO_3@FeO_x heterostructures manifest superior electrochemical performances as lithium-ion battery (LIB) anode materials. A high specific capacity of 913 mA h g^{-1} can be obtained after 100 cycles at 200 mA g^{-1}. Even tested at 1000 mA g^{-1}, the α-MoO_3@FeO_x heterostructures can be cycled stably, delivering a capacity of 540 mA h g^{-1} after 100 cycles.

RESULTS AND DISCUSSION

The synthesis of heterostructured α-MoO_3@FeO_x nanobelts is based on the simultaneous hydrolysis and oxidation of Fe^{2+} in aqueous solution in the presence of α-MoO_3 nanobelts. This process can be described as the following reactions:

Received: September 7, 2017
Accepted: October 26, 2017
Published: October 26, 2017

DOI: 10.1021/acsami.7b13529
ACS Appl. Mater. Interfaces 2017, 9, 39425−39431

$$Fe^{2+} + 2H_2O \rightarrow Fe(OH)_2 + 2H^+ \quad (1)$$

$$4Fe(OH)_2 + O_2 + 2H_2O \rightarrow 4Fe(OH)_3 \quad (2)$$

$$Fe(OH)_2 \rightarrow FeO + H_2O \quad (3)$$

$$2Fe(OH)_3 \rightarrow Fe_2O_3 + 3H_2O \quad (4)$$

XRD patterns of α-MoO_3@FeO_x and α-MoO_3 nanobelts are shown in Figure 1. The diffraction peaks of α-MoO_3 synthesized by hydrothermal method can be assigned to orthorhombic α-MoO_3 (JCPDS 35-0669). No impurity peaks can be observed, demonstrating the high purity of the α-MoO_3 nanobelts. The XRD pattern of α-MoO_3@FeO_x is similar to that of as-synthesized α-MoO_3. All the diffraction peaks can be assigned to α-MoO_3 while no peaks from FeO_x can be observed, suggesting that the FeO_x exists in an amorphous state. It is noted that the α-MoO_3 nanobelts exhibit much stronger (020) and (040) diffraction peaks than those of α-MoO_3@FeO_x and the standard card, which can be ascribed to the preferential orientation of α-MoO_3 nanobelts.[13,14] Because of their thinness, most α-MoO_3 nanobelts tend to lie on the bottom {010} surfaces (Figure S1, Supporting Information), leading to strengthened (0k0) diffractions, while, for the α-MoO_3@FeO_x, the thickness of the nanobelts increases, and more nanobelts tend to stand on their side (100) surfaces. Thus, the XRD pattern of α-MoO_3@FeO_x nanobelts is more close to the standard card. The Mo/Fe mole ratio of the α-MoO_3@FeO_x heterostructure is determined to be 0.74:1.0 by ICP-AES, which is lower than the feeding ratio (0.29:1.0), indicating that the iron source is in excess.

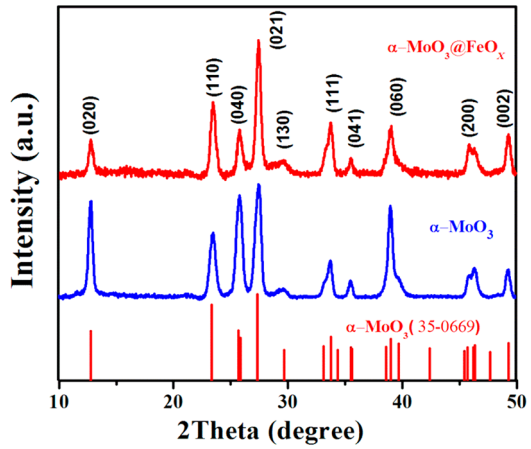

Figure 1. XRD patterns of the pristine α-MoO_3 and heterostructured α-MoO_3@FeO_x nanobelts.

The morphology and microstructure of the samples are investigated by SEM and TEM. The pristine α-MoO_3 (Figure S1, Supporting Information) shows a nanobelt morphology with smooth surface. The widths and lengths of the nanobelts are 200−250 nm and several micrometers, respectively. Detailed TEM and SAED characterization on a typical α-MoO_3 nanobelt reveals that the single-crystalline α-MoO_3 nanobelt grows along the [001] direction; the top and bottom surfaces of the nanobelts are of the {010} facets while the side surfaces are of the {100} and {001} facets. After treating with ammonium ferrous sulfate at 70 °C, numerous FeO_x nanoparticles are unevenly deposited on the surfaces of the 1D α-MoO_3 nanobelts, resulting in an increased diameter of 250−350 nm (Figure 2a−c). Compared with the bare α-MoO_3, the α-MoO_3@FeO_x nanobelt shows a much rougher surface, and the FeO_x nanoparticles mainly grow on the side surfaces of the α-MoO_3 nanobelts (Figure 2d). The HRTEM image (Figure 2e) exhibits the lattice fringes with an interlayer distance of 0.40 nm, corresponding to the {100} atomic spacings of α-MoO_3. The HRTEM result of the interfacial region between FeO_x and α-MoO_3 is shown in Figure S2. It is clear that the FeO_x is amorphous, while the α-MoO_3 is crystalline. The SAED pattern of α-MoO_3@FeO_x (Figure 2f) can be indexed to the [010] zone axis of α-MoO_3, suggesting that the α-MoO_3 in the heterostructure is single-crystalline while the FeO_x is generally amorphous.

The elemental distribution of the α-MoO_3@FeO_x is further studied by EDS element mapping, and the results are shown in Figure 3. It is apparent that the Mo and O distribute homogeneously in the core region. Nevertheless, the Fe

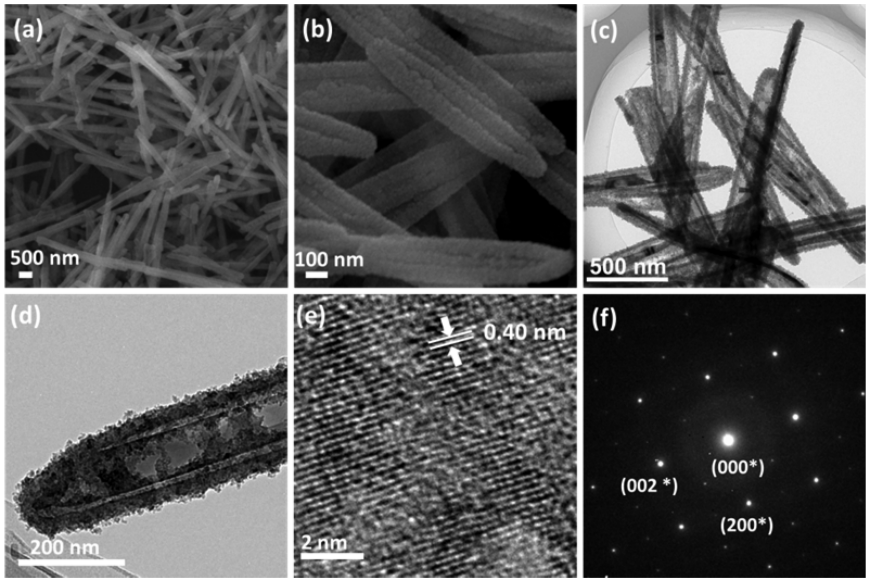

Figure 2. SEM images (a, b), TEM images (c, d), HRTEM image (e), and SAED pattern (f) of the α-MoO_3@FeO_x nanobelts.

DOI: 10.1021/acsami.7b13529
ACS Appl. Mater. Interfaces 2017, 9, 39425−39431

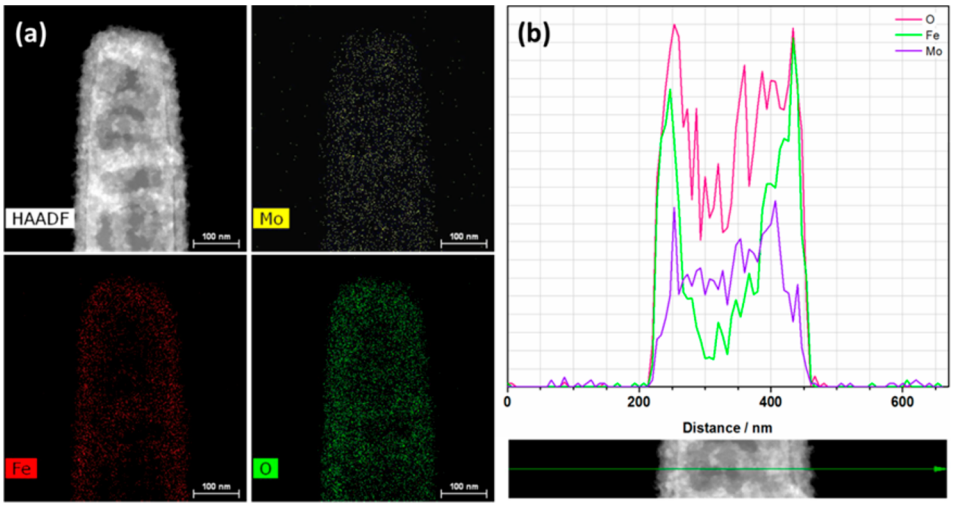

Figure 3. EDS element mappings (a) and EDS line scan (b) of the α-MoO_3@FeO_x nanobelt.

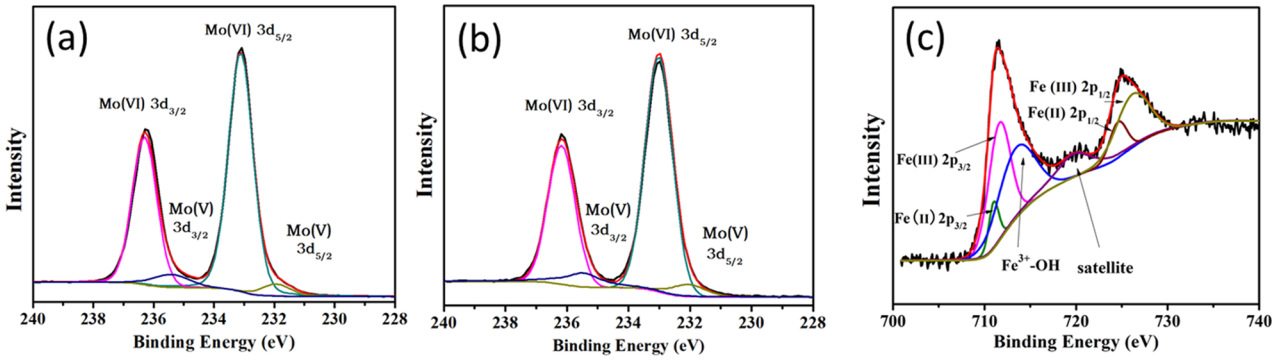

Figure 4. Mo 3d XPS spectrum of the α-MoO_3 (a). Mo 3d XPS spectrum of the α-MoO_3@FeO_x (b). Fe 2p XPS spectrum of the α-MoO_3@FeO_x (c).

distributes unevenly; the side surfaces are rich in Fe while the top and bottom surfaces are poor in Fe.

For determination of the valence states of products, XPS measurements are carried out. The Mo 3d spectrum of α-MoO_3 presents two 5/2−3/2 spin−orbit doublets. The dominant doublet peaks at binding energies of 233.1 and 236.3 eV correspond to Mo^{6+} $3d_{5/2}$ and $3d_{3/2}$ (Figure 4a), while the weak doublet peaks at lower binding energies of 231.8 and 234.9 eV can be ascribed to Mo^{5+} $3d_{5/2}$ and $3d_{3/2}$ (Figure 4a). Those binding energies are consistent with the previously reported literature values.[15] Similarly, two spin−orbit doublets are observed for α-MoO_3@FeO_x (Figure 4b). Just like for the pristine α-MoO_3, the intense Mo^{6+} $3d_{5/2}$ and $3d_{3/2}$ doublet peaks are sited at 233.1 and 236.3 eV, while the weak Mo^{5+} $3d_{5/2}$ and $3d_{3/2}$ doublet peaks are centered at 231.8 and 234.9 eV. Figure 4c show the Fe 2p XPS spectrum of α-MoO_3@FeO_x. The core separate peaks sited at 711.6 and 726.1 eV are associated with Fe^{3+} $2p_{3/2}$ and $2p_{1/2}$, respectively. Meanwhile, the intense satellite peak at around 719.7 eV can be attributed to a typical character of Fe^{3+}. Aside from the Fe^{3+} peaks, two strong doublet peaks of Fe 2p appear at 711.0 and 724.6 eV, which can be ascribed to Fe^{2+}.[16,17] Moreover, the peak at 713.5 eV may be indexed to Fe^{3+} bonded to hydroxyl groups.[18] Therefore, the Fe in the as-obtained MoO_3@FeO_x exists as Fe^{3+} and Fe^{2+}, indicating that Fe^{2+} has been partially oxidized to Fe^{3+}. As shown in Figure 4, the valence states of Mo did not change after FeO_x deposition, while the Fe^{2+} was partial oxidized to Fe^{3+}, suggesting that the Fe^{2+} was oxidized by the oxygen dissolved in solution rather than the α-MoO_3. Considering that no discernible chemical shift can be detected in the Mo 3d XPS spectra, it is speculated that no strong chemical bonding forms between α-MoO_3 and FeO_x. The interaction between α-MoO_3 and FeO_x would be the attraction between the oxygen lattice and Fe^{2+}/Fe^{3+}.

The formation process of α-MoO_3@FeO_x is proposed in Figure 5a on the basis of time-dependent experiments. The α-MoO_3 nanobelts prepared by hydrothermal method are enclosed by the {010}, {100}, and {001} facets. At the early stage of reaction (0.5 h), the FeO_x nanoparticles selectively deposit on the {001} and {100} facets of α-MoO_3 nanobelts, leaving the {010} facets uncovered (Figure 5b,c). With a prolonged reaction time (1.0 h), the FeO_x continues to grow on the {001} and {100} facets, forming a thin and continuous shell (Figure 5d,e). With further increased reaction time (2.0 h), the growth of FeO_x nanoparticles gradually propagates to the {010} facets (Figure 5f,g). The preferential deposition of FeO_x on the α-MoO_3 nanobelts is correlated to the surface energy of different crystal facets. For α-MoO_3, the surface energies of {001} and {100} facets are higher than that of the {010} facets according to Donnay−Harker rules.[19] To lower the total energy, the FeO_x nanoparticles deposit on the high-energy surfaces preferentially.

Both molybdenum oxides[13,14,20−22] and iron oxides[23−26] are promising electrode materials for lithium storage. For

DOI: 10.1021/acsami.7b13529
ACS Appl. Mater. Interfaces 2017, 9, 39425−39431

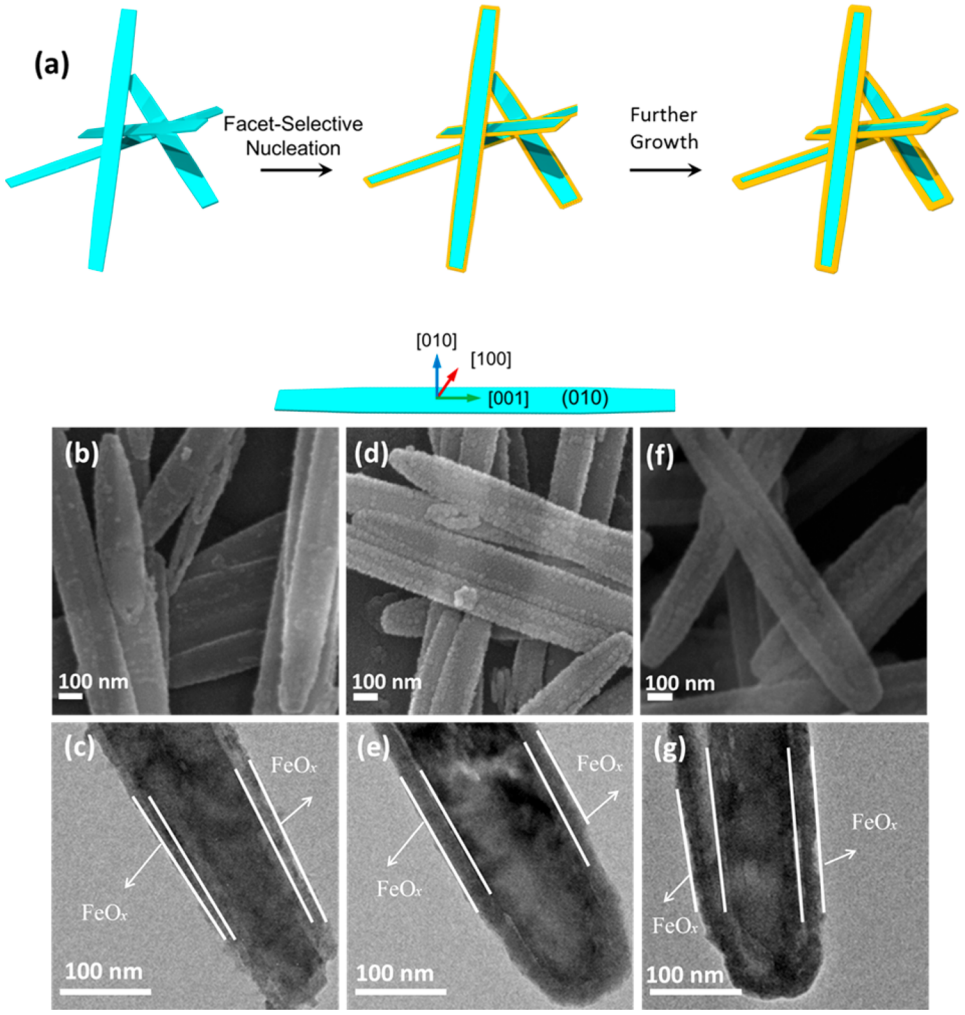

Figure 5. Schematic illustration for the formation of heterostructured α-MoO_3@FeO_x nanobelts (a). SEM and TEM images of α-MoO_3−FeO_x−0.5 (b, c), α-MoO_3−FeO_x−1.0 (d, e), and α-MoO_3−FeO_x−2.0 (f, g).

evaluation of their electrochemical performance, the α-MoO_3@FeO_x heterostructures are applied as the LIB anode. Figure S3 shows the cyclic voltammetry (CV) curves of α-MoO_3@FeO_x at a scan rate of 0.2 mV s^{-1} in a potential window 0.005−3.0 V. Three well-defined reduction peaks appear at 1.27, 0.68, and 0.27 V in the first cathodic process. The cathodic peak located at 1.27 V is probably caused by the lithium intercalation in MoO_3 ($MoO_3 + xLi^+ + xe^- \rightarrow Li_xMoO_3$).[27] The peak located at 0.68 V results from the irreversible formation of a solid electrolyte interface (SEI) layer accompanied by the reduction of Fe^{3+} and Fe^{2+}.[28−30] This peak shifts to 0.72 V in the subsequent cycles, and its intensity drops significantly. The peak at 0.27 V can be ascribed to the reduction of Li_xMoO_3 to metallic Mo.[31] In the first anodic process, a broad oxidation peak appears at 1.47 V, corresponding to the oxidation of reduced Mo and Fe species.[32] For comparison, the CV curves of pristine α-MoO_3 are shown in Figure S4a. Compared to that of α-MoO_3@FeO_x, the cathodic peak associated with Fe^{3+} and Fe^{2+} reduction disappears.

The galvanostatic discharge−charge cycling measurements are conducted at 200 mA g^{-1}. The α-MoO_3@FeO_x exhibits initial and second discharge capacities of 1338 and 735 mA h g^{-1} at 200 mA g^{-1} (Figure 6a). The irreversible capacity loss is ascribed to the SEI film formation on the electrode surface. The discharge capacity increases slowly with cycling, reaching 1154 mA h g^{-1} after 200 cycles (Figure 6b). A similar phenomenon, that is, capacity increase with cycling, has been frequently observed in iron oxide based anode materials.[33] According to the previous literature, such capacity increase can be attributed to the polymeric gel-like film resulted from electrolyte deposition which can reversibly grow/dissolve.[34,35] The initial Coulombic efficiency is 72%; for the subsequent cycles, the Coulombic efficiency reaches almost 100% (Figure S5). For the pristine α-MoO_3, it exhibits an initial discharge capacity of 1023 mA h g^{-1} and an initial Coulombic efficiency of 65% (Figure S4b and Figure S5). At a current density of 200 mA g^{-1}, the specific capacity decays to 160 mA h g^{-1} at 200 cycles. Figure 6c shows the cyclability of α-MoO_3@FeO_x and α-MoO_3 at a higher current density, 1000 mA g^{-1}. After 100 cycles at 1000 mA g^{-1}, a capacity of 540 mA h g^{-1} is achieved for α-MoO_3@FeO_x, much higher than that of pristine α-MoO_3 (220 mA h g^{-1}). The superior cyclability of α-MoO_3@FeO_x indicates its better structural stability for long-term cycling, which originates from the strain relaxation ability of the amorphous FeO_x coating layer.[36,37]

For elucidation of the effect of reaction time on the electrochemical performance, a series of α-MoO_3@FeO_x nanobelts were prepared by adjusting the reaction time from 0.5 to 6 h (α-MoO_3−FeO_x−0.5, α-MoO_3−FeO_x−2.0, α-MoO_3−FeO_x−6.0, and α-MoO_3@FeO_x with a reaction time

DOI: 10.1021/acsami.7b13529
ACS Appl. Mater. Interfaces 2017, 9, 39425−39431

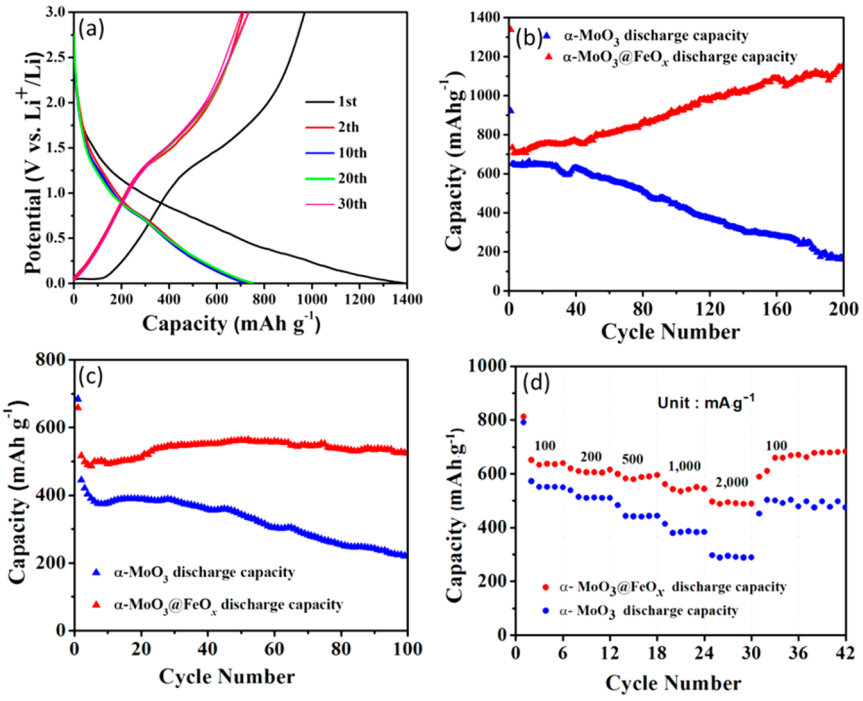

Figure 6. Galvanostatic discharge−charge voltage profiles of the α-MoO_3@FeO_x nanobelts at 200 mA g^{-1} (a). Cycling performance of the α-MoO_3 and α-MoO_3@FeO_x nanobelts at 200 (b) and 1000 (c) mA g^{-1}. Rate performance of the α-MoO_3 and α-MoO_3@FeO_x nanobelts (d).

of 4 h). The cycling performances of the samples and α-MoO_3@FeO_x are shown in Figure S6. Among all the samples, the α-MoO_3@FeO_x with a reaction time of 4 h demonstrates the best electrochemical performance in terms of cycling stability and specific capacity.

To investigate the effects of annealing, the α-MoO_3@FeO_x composite was annealed in air at 400 °C for 4 h, and the product was denoted as α-MoO_3−FeO_x−400. The SEM and TEM images, XRD patterns, as well as cycling performance of α-MoO_3−FeO_x−400 are shown in Figure S7. The morphology and microstructure of the α-MoO_3−FeO_x−400 are similar to those of the α-MoO_3@FeO_x nanobelts, indicating the good structural integrity of α-MoO_3@FeO_x (Figure S7a,b). No peaks of iron oxide can be detected in the XRD pattern of α-MoO_3−FeO_x−400 (Figure S7c), suggesting that the FeO_x does not crystallize during annealing at 400 °C. The α-MoO_3−FeO_x−400 exhibits initial and second discharge capacities of 1053 mA h $g^{-1}$and 765 mA h g^{-1} at 200 mA g^{-1} (Figure S7d). The capacity drops to 515 mA h g^{-1} at the 40th cycle. Then, the discharge capacity increases slowly with cycling, reaching 580 mA h g^{-1} after 100 cycles.

The rate performances of α-MoO_3 and α-MoO_3@FeO_x nanobelts are studied by varying the current density from 100 to 2000 mA g^{-1} (Figure 6d). The α-MoO_3@FeO_x delivers average capacities of ca. 650, 600, 580, and 530 mA h g^{-1} at 100, 200, 500, and 1000 mA g^{-1}, respectively. Even at a high current density of 2000 mA g^{-1}, a specific capacity of ca. 490 mA h g^{-1} can be achieved. Compared to that of α-MoO_3@FeO_x, the rate performance of α-MoO_3 is unsatisfactory. The average discharge capacities at 100, 200, 500, 1000, and 2000 mA g^{-1} are ∼550, 500, 440, 380, and 290 mA h g^{-1}, respectively.

Electrochemical impedance spectroscopy (EIS) is carried out to investigate the kinetic behaviors of the α-MoO_3 and α-MoO_3@FeO_x electrodes. Both Nyquist plots are constituted of a depressed semicircle in the high-frequency region and a slope line in the low-frequency region (Figure S8). The radius of the semicircle reflects the charge transfer resistance (R_{ct}) at the electrolyte/electrode interface. The R_{ct} value for α-MoO_3@FeO_x is calculated to be 78 Ω, which is much lower than that of pristine α-MoO_3 (460 Ω). Considering that the electrons always flow from conduction bands with higher energy to those with lower energy in semiconductor heterojunctions, the enhanced charge transfer of α-MoO_3@FeO_x could possibly be ascribed to the different band structures of α-MoO_3 and FeO_x.

On the basis of the above analyses, the superior electrochemical performances of heterostructured α-MoO_3@FeO_x nanobelts can be ascribed to the following aspects: (I) Both FeO_x and α-MoO_3 nanobelts possess a high theoretical capacity. (II) The amorphous feature of FeO_x is beneficial for strain relaxation and volume expansion accommodation during lithiation/delithiation, leading to better structural stability and thus cycling performance. (III) Because of their difference in electronic band structures, the deposition of FeO_x on α-MoO_3 nanobelts facilitates the electron transfer, which is helpful to the rate capability.

CONCLUSION

In summary, a facile facet-selective deposition strategy has been developed for the construction of heterostructured α-MoO_3@FeO_x nanobelts. Because of the anisotropic feature of α-MoO_3 nanobelts, the FeO_x preferentially deposits on the (100) and (001) facets of α-MoO_3 nanobelts. The deposition of FeO_x on α-MoO_3 would facilitate the electron transfer. As a result, the heterostructured α-MoO_3@FeO_x nanobelts exhibit superior lithium storage performances. It is expected that the facet-selective deposition strategy would be extended to the construction of other novel 1D, 2D, and 3D heterostructures with fascinating physical/chemical properties and wide potential applications.

DOI: 10.1021/acsami.7b13529
ACS Appl. Mater. Interfaces 2017, 9, 39425−39431

■ ASSOCIATED CONTENT

Supporting Information

The Supporting Information is available free of charge on the ACS Publications website at DOI: 10.1021/acsami.7b13529.

Nanobelt synthesis details, material characterizations, electrochemical measurements, scanning electron microscopy (SEM) results, transmission electron microscopy (TEM) results, galvanostatic discharge−charge voltage profiles, HRTEM image, Coulombic efficiency values, CV curves, EIS results, XRD results, and cycle performances with comparisons (PDF)

■ AUTHOR INFORMATION

Corresponding Authors

*E-mail: liangzhou@whut.edu.cn.

*E-mail: mlq518@whut.edu.cn.

ORCID

Zechao Zhuang: 0000-0002-0050-9574

Liang Zhou: 0000-0001-6756-3578

Liqiang Mai: 0000-0003-4259-7725

Author Contributions

§Y.Y. and N.X. contributed equally to this work. The manuscript was written through contributions of all authors. All authors have given approval to the final version of the manuscript.

Notes

The authors declare no competing financial interest.

■ ACKNOWLEDGMENTS

This work was supported by the National Key Research and Development Program of China (2016YFA0202603), the National Basic Research Program of China (2013CB934103), the Programme of Introducing Talents of Discipline to Universities (B17034), the National Natural Science Foundation of China (51521001, 21673171, 51502226), the National Natural Science Fund for Distinguished Young Scholars (51425204), and the Fundamental Research Funds for the Central Universities (WUT: 2016III001, 2016III002, 2017III009, 2017III008).

■ REFERENCES

(1) Lauhon, L. J.; Gudiksen, M. S.; Wang, D.; Lieber, C. M. Epitaxial Core−Shell and Core−Multishell Nanowire Heterostructures. *Nature* **2002**, *420*, 57−61.

(2) Wu, Y.; Xiang, J.; Yang, C.; Lu, W.; Lieber, C. M. Single-Crystal Metallic Nanowires and Metal/Semiconductor Nanowire Heterostructures. *Nature* **2004**, *430*, 61−65.

(3) Tang, J.; Huo, Z.; Brittman, S.; Gao, H.; Yang, P. Solution-Processed Core-Shell Nanowires for Efficient Photovoltaic Cells. *Nat. Nanotechnol.* **2011**, *6*, 568−572.

(4) Xia, Y.; Yang, P.; Sun, Y.; Wu, Y.; Mayers, B.; Gates, B.; Yin, Y.; Kim, F.; Yan, H. One-Dimensional Nanostructures: Synthesis, Characterization, and Applications. *Adv. Mater.* **2003**, *15*, 353−389.

(5) Mai, L.; Tian, X.; Xu, X.; Chang, L.; Xu, L. Nanowire Electrodes for Electrochemical Energy Storage Devices. *Chem. Rev.* **2014**, *114*, 11828−11862.

(6) Mai, L.; Zhang, Q.; Nan, C. W. Materials Research at Wuhan University of Technology. *Adv. Mater.* **2017**, *29*, 29.

(7) Gu, X.; Chen, L.; Ju, Z.; Xu, H.; Yang, J.; Qian, Y. Controlled Growth of Porous α-Fe_2O_3 Branches on β-MnO_2 Nanorods for Excellent Performance in Lithium-Ion Batteries. *Adv. Funct. Mater.* **2013**, *23*, 4049−4056.

(8) Mai, L.-Q.; Yang, F.; Zhao, Y.-L.; Xu, X.; Xu, L.; Luo, Y.-Z. Hierarchical $MnMoO_4$/$CoMoO_4$ Heterostructured Nanowires With Enhanced Supercapacitor Performance. *Nat. Commun.* **2011**, *2*, 381.

(9) Ding, S.; Chen, J. S. One-Dimensional Hierarchical Structures Composed of Novel Metal Oxide Nanosheets on A Carbon Nanotube Backbone and Their Lithium-Storage Properties. *Adv. Funct. Mater.* **2011**, *21*, 4120−4125.

(10) Xia, X.; Tu, J.; Zhang, Y.; Wang, X.; Gu, C.; Zhao, X.-b.; Fan, H. J. High-Quality Metal Oxide Core/Shell Nanowire Arrays on Conductive Substrates for Electrochemical Energy Storage. *ACS Nano* **2012**, *6*, 5531−5538.

(11) Xia, X.; Tu, J.; Zhang, Y.; Chen, J.; Wang, X.; Gu, C.; Guan, C.; Luo, J.; Fan, H. J. Porous Hydroxide Nanosheets on Preformed Nanowires by Electrodeposition: Branched Nanoarrays for Electrochemical Energy Storage. *Chem. Mater.* **2012**, *24*, 3793−3799.

(12) Zhou, C.; Zhang, Y.; Li, Y.; Liu, J. Construction of High-Capacitance 3D CoO@ Polypyrrole Nanowire Array Electrode for Aqueous Asymmetric Supercapacitor. *Nano Lett.* **2013**, *13*, 2078−2085.

(13) Zhou, L.; Yang, L.; Yuan, P.; Zou, J.; Wu, Y.; Yu, C. α-MoO_3 Nanobelts: A High Performance Cathode Material for Lithium Ion Batteries. *J. Phys. Chem. C* **2010**, *114*, 21868−21872.

(14) Mai, L. Q.; Hu, B.; Chen, W.; Qi, Y.; Lao, C.; Yang, R.; Dai, Y.; Wang, Z. L. Lithiated MoO_3 Nanobelts with Greatly Improved Performance for Lithium Batteries. *Adv. Mater.* **2007**, *19*, 3712−3716.

(15) Swiatowska-Mrowiecka, J.; de Diesbach, S.; Maurice, V.; Zanna, S.; Klein, L.; Briand, E.; Vickridge, I.; Marcus, P. Li-Ion Intercalation in Thermal Oxide Thin Films of MoO_3 as Studied by XPS, RBS, and NRA. *J. Phys. Chem. C* **2008**, *112*, 11050−11058.

(16) Bhargava, G.; Gouzman, I.; Chun, C.; Ramanarayanan, T.; Bernasek, S. Characterization of the "Native" Surface Thin Film on Pure Polycrystalline Iron: A High Resolution XPS and TEM Study. *Appl. Surf. Sci.* **2007**, *253*, 4322−4329.

(17) An, Q.; Lv, F.; Liu, Q.; Han, C.; Zhao, K.; Sheng, J.; Wei, Q.; Yan, M.; Mai, L. Amorphous Vanadium Oxide Matrixes Supporting Hierarchical Porous Fe_3O_4/Graphene Nanowires as A High-Rate Lithium Storage Anode. *Nano Lett.* **2014**, *14*, 6250−6256.

(18) Yang, S.; Guo, Y.; Yan, N.; Wu, D.; He, H.; Qu, Z.; Jia, J. Elemental Mercury Capture from Flue Gas by Magnetic Mn−Fe Spinel: Effect Of Chemical Heterogeneity. *Ind. Eng. Chem. Res.* **2011**, *50*, 9650−9656.

(19) Donnay, J. D. H.; Harker, D. A New Law of Crystal Morphology Extending the Law of Bravais. *Am. Mineral.* **1937**, *22* (5), 446−467.

(20) Kim, H.-S.; Cook, J. B.; Lin, H.; Ko, J. S.; Tolbert, S. H.; Ozolins, V.; Dunn, B. Oxygen Vacancies Enhance Pseudocapacitive Charge Storage Properties of MoO_{3-x}. *Nat. Mater.* **2017**, *16*, 454−460.

(21) Tao, T.; Glushenkov, A. M.; Zhang, C.; Zhang, H.; Zhou, D.; Guo, Z.; Liu, H. K.; Chen, Q.; Hu, H.; Chen, Y. MoO_3 Nanoparticles Dispersed Uniformly in Carbon Matrix: A High Capacity Composite Anode for Li-Ion Batteries. *J. Mater. Chem.* **2011**, *21*, 9350−9355.

(22) Zhou, L.; Wu, H. B.; Wang, Z.; Lou, X. W. Interconnected MoO_2 Nanocrystals with Carbon Nanocoating as High-Capacity Anode Materials for Lithium-Ion Batteries. *ACS Appl. Mater. Interfaces* **2011**, *3*, 4853−4857.

(23) Zhang, L.; Wu, H. B.; Lou, X. W. D. Iron-Oxide-Based Advanced Anode Materials for Lithium-Ion Batteries. *Adv. Energy Mater.* **2014**, *4*, 1300958.

(24) Zhao, K.; Wen, M.; Dong, Y.; Zhang, L.; Yan, M.; Xu, W.; Niu, C.; Zhou, L.; Wei, Q.; Ren, W. Thermal Induced Strain Relaxation of 1D Iron Oxide for Solid Electrolyte Interphase Control and Lithium Storage Improvement. *Adv. Energy Mater.* **2017**, *7*, 1601582.

(25) Zhou, L.; Xu, H.; Zhang, H.; Yang, J.; Hartono, S. B.; Qian, K.; Zou, J.; Yu, C. Cheap and Scalable Synthesis of α-Fe_2O_3 Multi-Shelled Hollow Spheres as High-Performance Anode Materials for Lithium Ion Batteries. *Chem. Commun.* **2013**, *49*, 8695−8697.

(26) Zhang, H.; Zhou, L.; Noonan, O.; Martin, D. J.; Whittaker, A. K.; Yu, C. Tailoring the Void Size of Iron Oxide@ Carbon Yolk−Shell Structure for Optimized Lithium Storage. *Adv. Funct. Mater.* **2014**, *24*, 4337−4342.

(27) Meduri, P.; Clark, E.; Kim, J. H.; Dayalan, E.; Sumanasekera, G. U.; Sunkara, M. K. MoO_{3-x} Nanowire Arrays as Stable and High-Capacity Anodes for Lithium Ion Batteries. *Nano Lett.* **2012**, *12*, 1784−1788.
(28) Shirakawa, J.; Nakayama, M.; Wakihara, M.; Uchimoto, Y. Changes In Electronic Structure Upon Lithium Insertion into $Fe_2(SO_4)_3$ and $Fe_2(MoO_4)_3$ Investigated by X-Ray Absorption Spectroscopy. *J. Phys. Chem. B* **2007**, *111*, 1424−1430.
(29) Han, F.; Ma, L.; Sun, Q.; Lei, C.; Lu, A. Rationally Designed Carbon-Coated Fe_3O_4 Coaxial Nanotubes with Hierarchical Porosity as High-Rate Anodes for Lithium Ion Batteries. *Nano Res.* **2014**, *7*, 1706−1717.
(30) Liu, H.; Wang, G.; Park, J.; Wang, J.; Liu, H.; Zhang, C. Electrochemical Performance of α-Fe_2O_3 Nanorods as Anode Material For Lithium-Ion Cells. *Electrochim. Acta* **2009**, *54*, 1733−1736.
(31) Wang, Q.; Sun, J.; Wang, Q.; Zhang, D.-a.; Xing, L.; Xue, X. Electrochemical Performance of α-MoO_3−In_2O_3 Core−Shell Nanorods As Anode Materials for Lithium-Ion Batteries. *J. Mater. Chem. A* **2015**, *3*, 5083−5091.
(32) Morales, J.; Sánchez, L.; Martín, F.; Berry, F.; Ren, X. Synthesis and Characterization of Nanometric Iron and Iron-Titanium Oxides by Mechanical Milling: Electrochemical Properties as Anodic Materials in Lithium Cells. *J. Electrochem. Soc.* **2005**, *152*, A1748−A1754.
(33) Zhou, G.; Wang, D.-W.; Li, F.; Zhang, L.; Li, N.; Wu, Z.-S.; Wen, L.; Lu, G. Q.; Cheng, H.-M. Graphene-Wrapped Fe3O4 Anode Material with Improved Reversible Capacity and Cyclic Stability for Lithium Ion Batteries. *Chem. Mater.* **2010**, *22*, 5306−5313.
(34) Laruelle, S.; Grugeon, S.; Poizot, P.; Dolle, M.; Dupont, L.; Tarascon, J. On the Origin of the Extra Electrochemical Capacity Displayed by Mo/Li Cells At Low Potential. *J. Electrochem. Soc.* **2002**, *149*, A627−A634.
(35) Grugeon, S.; Laruelle, S.; Dupont, L.; Tarascon, J.-M. An Update On the Reactivity of Nanoparticles Co-Based Compounds Towards Li. *Solid State Sci.* **2003**, *5*, 895−904.
(36) Xu, Y.; Zhou, M.; Zhang, C.; Wang, C.; Liang, L.; Fang, Y.; Wu, M.; Cheng, L.; Lei, Y. Oxygen Vacancies: Effective Strategy to Boost Sodium Storage of Amorphous Electrode Materials. *Nano Energy* **2017**, *38*, 304.
(37) Zhou, T.; Zheng, Y.; Gao, H.; Min, S.; Li, S.; Liu, H. K.; Guo, Z. Surface Engineering and Design Strategy for Surface-Amorphized TiO_2@Graphene Hybrids for High Power Li-Ion Battery Electrodes. *Adv. Sci.* **2015**, *2*, 1500027.

DOI: 10.1021/acsami.7b13529
ACS Appl. Mater. Interfaces 2017, 9, 39425−39431